Virtual study to investigate the detectability of breast abnormalities on 2D mammography and digital breast tomosynthesis

Kristina Tri Wigati[1,2], Hannah Manssens[3], Liesbeth Vancoillie[2], Lesley Cockmartin[4], Djarwani S. Soejoko[1], Hilde Bosmans[2,4], and Kristina Bliznakova[5]

[1] *Department of Physics, Faculty of Mathematics and Natural Sciences, University of Indonesia*
[2] *Department of Imaging and Pathology, Faculty of Medicine, KU Leuven*
[3] *Barco nv, Belgium*
[4] *Department of Radiology, University Hospitals Leuven*
[5] *Laboratory of Computer Simulations in Medicine, Technical University of Varna*

E-mail: kristina.tw@ui.ac.id

Received August 11 2017
Revised December 06 2017
Accepted for publication February 12 2018
Published March 05 2018

Abstract: This paper describes the use of virtual clinical trial software, as developed and improved in the frame of the Horizon2020 MaXIMA project, to study particular aspects of 2D mammography and digital breast tomosynthesis. A voxel-based breast phantom with inserted mathematical models of an irregular mass and two microcalcifications was created. Image acquisition was simulated by using XRAYImagingSimulator, while image reconstruction was accomplished with FDKR software. Series of images were created for different angular ranges with an identical total dose. Detectability of the abnormalities was investigated using visual assessment and quantitative measurements. The results agree with other studies in literature studying the same aspects and therefore confirm the value of the new framework for other future applications.

Keywords*: computational phantom, mass, microcalcifications, virtual clinical trial*

1. Introduction

Nowadays, the advanced medical imaging technologies use virtual studies during pre-clinical system development.[1-8] Next to physical phantoms, computational phantoms that mimic human anatomical features are used as well.[9-13] In breast imaging applications, the physical phantoms currently used are limited in representing the variety of breast sizes, shapes, compositions, and parenchymal detail. Their limitations are mostly related to the expense of composed materials and time efficiency in generating patient-specific physical phantoms.[14] Therefore, a computational phantom can be an alternative choice.

The computational breast phantom can be created either based on mathematical breast models with geometric primitives, or using voxelization of real patient data. The mathematical breast phantom offers flexibility to be modified into various compositions of breasts, but its geometrical simplicity may not represent the real breast tissue. On the other hand, the voxelized breast phantom offers a more realistic model since it is based on actual clinical data, but as created from individual breast data, it may not represent the variability in the whole population. The computational phantoms are used in combination with Monte Carlo codes to simulate radiation beam transport. Image processing is then applied on simulated images prior to signal analysis. This combination of image formation and analysis can be referred as a virtual study and has high potential benefit for medical imaging application during pre-, ongoing, and post-clinical implementation in terms of development, optimization and evaluation purposes[15-21], particularly in breast imaging that is the focus of this project.

To date, two-dimensional (2D) mammography remains the gold standard imaging technique for screening and diagnosis of breast cancer. Digital mammography has overcome many of the technical limitations of screen film

mammography. However, the 2D projection that happens during normal imaging of a three-dimensional (3D) object induces tissue superposition, which can reduce the visibility of the abnormal tissue (false negative findings) and lead to unnecessary recalls (false positive findings), especially in dense breasts. Digital breast tomosynthesis (DBT), a pseudo-tomographic imaging technique, has been developed to address this superposition problem.[1,22]

A DBT system is a modified digital mammography system with the X-ray tube moving along an arc and generating a series of projection images while the compressed breast remains stationary (Figure 1). During the acquisitions, the detector can either be static or dynamic in order to maintain its orientation to the X-ray tube. Typically, a small number (9-25) of low dose projection images are obtained over a limited range of angles (±7° to ±30°), and reconstructed into a 3D volume using filtered back projection (FBP) or an iterative reconstruction algorithm.

While the DBT system can indeed reduce the superposition problem, it should be considered that its spatial resolution is anisotropic: higher in-plane resolution (x-axis and y-axis) and relatively poor resolution between planes (z-axis). In fact, due to the limited angular range, the reconstructed images do not represent the realistic 3D breast anatomy. Therefore, the factors that impact acquisition geometry, including the number of projections, the total angular range covered by the projections, and the distribution of the projections, are essential and have to be investigated.[22-24] Prior to the approval of DBT to replace the 2D mammography, these issues – and many more – have to be addressed.

A *virtual clinical trial* can be an efficient method to investigate the aforementioned issues. In this paper, we perform a first virtual clinical study for the investigation of the detectability of breast abnormalities on 2D mammography and DBT, for various angular ranges and numbers of projections.

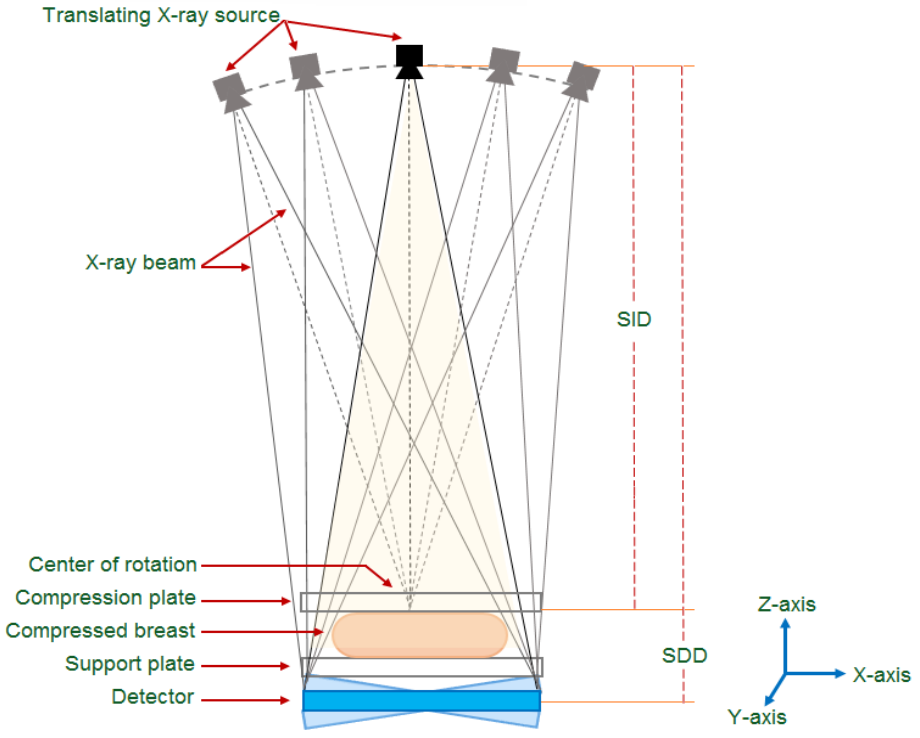

Figure 1. Digital breast tomosynthesis: a modified digital mammography system in which the X-ray tube pivots about a point (center of rotation) close or on the detector surface, while the detector can be static or rotate depending on the system design. SID and SDD are source-to-center of rotation and source-to-detector distances. In this study, the SID and SDD were set at 600 mm and 660 mm respectively.

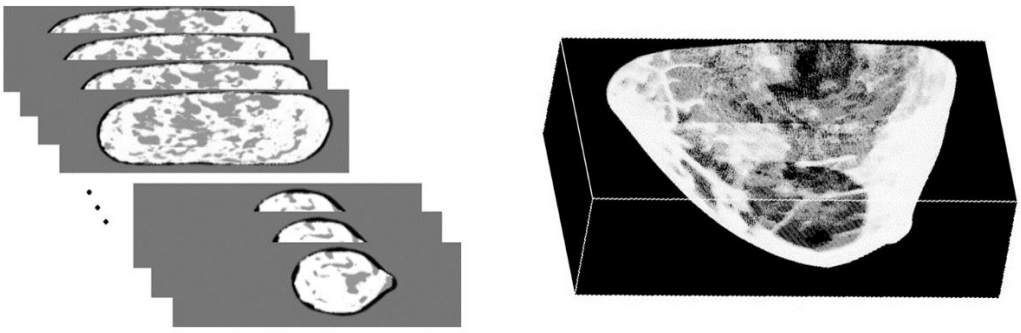

Figure 2. Computational breast phantom used in the study: (a) Compressed breast CT slices and (b**)** The composed voxel-based breast phantom with dimensions of 173 mm (width) × 123 mm (length) × 47 mm (height).

2. Materials and methods

2.1. The XRAYImagingSimulator software

The XRAYImagingSimulator[25] is an in-house developed application used to model various x-ray imaging techniques and to simulate the interaction of the x-rays through the modeled system. The simulator is composed of several modules which provide different functionalities: phantom modeling, scanning geometry and image formation modeling as well as visualization possibilities. The computational phantoms are modeled as a synthesis of geometrical (ellipsoids, cylinders, cubes, etc) or voxelized primitives (from patient images). In the latter case, each voxel from the phantom carries information for the tissue composition. The scanning geometry is modeled by using parameters such as distances from the source to the center of rotation and to the detector, gantry angle arc and step, as well as imaging and some beam parameters. Image formation simulation concerns modeling of the x-rays through the modeled x-ray system. This formation may be accomplished either analytically or by Monte Carlo techniques. In this study, we used the first approach, where the simulation uses analytical relationships for X-ray matter interaction that does not take into account scattering events in the modeled parts.

2.2. Creating the breast phantom

In our approximation, the normal breast consists of glandular, fibrous, and adipose tissue, positioned over the pectoral muscles and attached to the chest wall by fibrous strands (Cooper's ligaments). Abnormal tissue includes abnormalities such as masses and/or microcalcifications. The abnormalities have different characteristics such as size, shape, location, density, margins, number and distribution. Some of these features are associated with the lesion being either malignant or benign. As an example, a mass with well-circumscribed and regular margin, dimensions of less than 1.5 cm, and with a low density region is most likely classified as a benign lesion. While the malignant one can be identified by its indistinct margin, irregular contour, and high density. Benign microcalcifications have a uniform shape and density, and are usually randomly distributed. Malignant microcalcifications are generally smaller than the benign, with an irregular shape, size, and distribution.[15]

In this study, a hybrid 3D voxel-based breast phantom based on both patient data and mathematical modeling was created. The background tissue of a normal breast was synthetized using real patient data, while the lesions, namely an irregular mass and two ellipsoid microcalcifications, were created with mathematical modeling.

2.2.1. Normal breast model (background)

The breast phantom simulated in this study is based on CT data from a real patient, made available for teaching and research purposes in the EUTEMPE-RX module 5. The CT slices are obtained from a dedicated breast CT scanner at the Department of Radiology and Imaging at Emory University (Atlanta, Georgia, USA). From the study of Yang *et al*[26], these data were de-noised and segmented in order to obtain the composition of skin, glandular, and adipose

tissue, as major parts in a normal breast model. To mimic the clinical application, the simulated normal breast was compressed. These compressed breast slices were then fused into a 3D volume using the *XRAYImagingSimulator* software with the attenuation data listed in Table 1. Finally, a voxel-based breast phantom with dimensions of 641×457×175 pixels^3 (resolution of 0.27 mm/pixel) was created (Figure 2).

2.2.2. Models of Abnormalities

- Mass

The irregular mass was generated using a 3D random walk algorithm according to the study of Hintsala *et al*[27]. The three modeling parameters are the size of the tumor matrix, the number of the random walks and the length of each walk. Each random walk starts from the center of the matrix and each step moves randomly to a neighbouring voxel, defining the mass attenuation coefficient (μ_{mass}). The matrix size, resolution, number of the random walks and length of each walk were set to 200×200×200 pixels^3, 0.27 mm/pixel, 100 and 1000, respectively. The random structure was converted into an irregular mass with solid geometry by using subsequently two morphological operations: dilation and erosion with a cubic structure element of size 4×4×4 pixels$^{3.}$ The final matrix model contains 0 and 1, where 1 corresponds to abnormality tissue. The computational model of the obtained irregular mass is shown in Figure 3. The voxelized irregular mass matrix was then put near to the center of the normal breast phantom.

Table 1. The composition of breast phantom elements (as percentage of weight), density and attenuation coefficients of the modeled breast structures at 20 keV incident energy. The voxel values for the simulated tissues are also specified.

Tissue	***Composition***	***Total mass attenuation (cm2/g)***	***Total linear attenuation (cm-1)***	***Density (g.cm-3)***	***Voxel value***
Breast skin	H: 0.100588; C: 0.228250; N: 0.046420; O: 0.619002; Na: 0.000070; Mg: 0.000060; P: 0.000330; S: 0.001590; Cl: 0.002670; K: 0.000850; Ca: 0.000150; Fe: 0.000010; Zn: 0.000010	0.75	0.81	1.09	1
Air	C: 0.000120; N: 0.755270; O: 0.231780; Ar: 0.012830	0.78	0.00	1.23×10^{-3}	20
Glandular tissue	H: 0.106000; C: 0.332000; N: 0.030000; O: 0.527000; Na: 0.001000; P: 0.001000; S: 0.002000; Cl: 0.001000	0.69	0.70	1.02	125
Adipose tissue	H: 0.119477; C: 0.637240; N: 0.007970; O: 0.232333; Na: 0.000500; Mn: 0.000020; P: 0.000160; S: 0.000730; Cl: 0.001190; K: 0.000320; Ca: 0.000020; Fe: 0.000020; Zn: 0.000020	0.55	0.51	0.92	200
Irregular mass	H_2O	0.81	0.81	1.00	201
Microcalcifications	$CaCO_3$	5.70	15.44	2.71	217

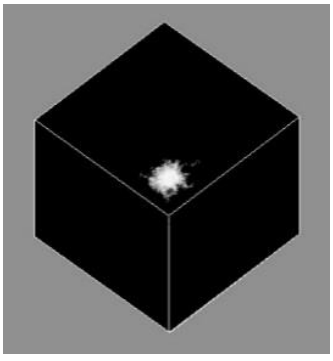

Figure 3. The irregular mass model.

- Microcalcifications

The voxelized version of two ellipsoid microcalcifications with dimensions 0.5×0.5×0.3 mm^3 (*Calc1*) and 0.5×0.6×0.4 mm^3 (*Calc2*) were inserted in the breast volume in two locations: *Calc1* was inserted in the center of the irregular mass, while *Calc2* was placed 5.8 mm apart from the *Calc1*. The microcalcifications composition was $CaCO_3$.

2.3. Image acquisition and processing

Simulation of mammographic images was also performed with the *XRAYImagingSimulator* software. Source-to-center of rotation and source-to-image receptor distances were set equal to 600 and 660 mm, respectively. A 20 keV monochromatic incident beam was used, and its penetration was calculated from the attenuation of successive layers using Beer-Lambert equation. An ideal stationary detector was modeled, i.e. a photon counting detector that absorbs all impinging x-rays, with a resolution of 10 pixels/mm. Scatter radiation was not included, making it effectively a study under scatter-free conditions. The synthetic images were projected with a size of 1000×1000 pixels^2. The settings of angular range and number of projection are shown in Table 2. The atomic compositions of the simulated breast tissues are derived from data of the International Commission on Radiation Units and Measurements and the International Commission on Radiological Protection (Table 1).

The incident air kerma at the surface of the breast models was set to 3.5 mGy and 7.0 mGy for 2D mammography and DBT simulation, respectively. The photon fluence was calculated from the following equation:

$$K_i = \left[\frac{\mu_{en}}{\rho}\right]_{air} E\Phi \tag{1}$$

where K_i is the incident air kerma, E is the energy of the incident photons, Φ is the photon fluence, and $\left[\mu_{en}/\rho\right]_{air}$ is the mass energy absorption coefficients of air.

Poisson quantum noise was generated using a Gaussian random number generator and then added into the ideal projection images. The noisy 2D image projected from 0° was then used for analyzing the 2D mammography in craniocaudal (CC) view, while other noisy projection images were used to reconstruct the DBT images.

For DBT image reconstruction, the in-house developed FDKR software was used.[4,28-29] The noisy projection images were filtered by the FBP algorithm (Ramp filter) before being reconstructed in a set of planes. A series of reconstructed slices in the form of a PNG file with size of 256 × 256 pixels^2 (resolution of 4.27 pixels/mm) was analyzed to study the DBT performance. The window range was set to a constant level (-0.040 to +0.015) over all DBT slices.

Table 2. The acquisition geometry. For DBT simulation, an incremental step of 2° was used for the projections.

System	*Angular range*	*Number of proj. Images*
2D mammography	0^0	1
DBT	$\pm 9^0$	10
	$\pm 13^0$	14
	$\pm 15^0$	16
	$\pm 21^0$	22
	$\pm 25^0$	26

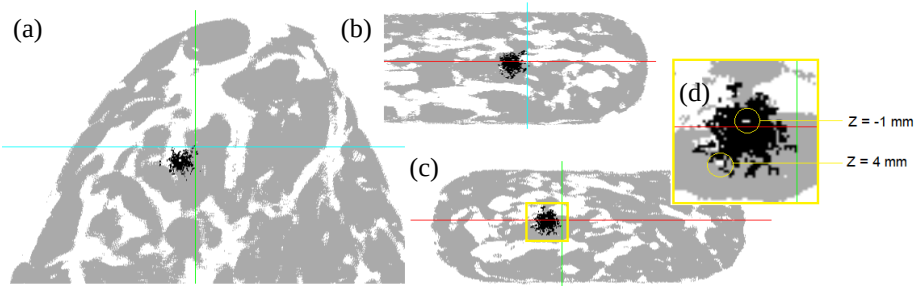

Figure 4. Compressed breast phantom from coronal (a), sagittal (b), and axial (c) view together with its inset (d) using the 3D viewer of ImageJ software. This image was captured to visualize the position of adipose tissue (gray), glandular tissue (white), irregular mass (black) and microcalcifications (white spot within irregular mass region) by adjusting brightness and contrast level. Figure (d) shows a microcalcification at Z = -1 mm and Z = 4 mm.

2.4. Image analysis

2.4.1. Qualitative assessment

Qualitative assessment was performed by simple visual inspection of all images synthesized in this study. The assessment was performed by two medical physicists and the final results were determined by consensus.

2.4.2. Quantitative measurement

Four figures of merit – *pixel value* (PV), *signal difference* (SD), *signal difference-to-noise ratio* (SDNR) and *percentage of contrast* (C) – were calculated in this study on both 2D and DBT images. The SD, SDNR and C were calculated using equation (2), (3), and (4) respectively.

$$SD = \left| PV_{abn} - PV_{bg} \right| \tag{2}$$

$$SDNR = \frac{SD}{\sigma_{bg}} \tag{3}$$

$$C = \frac{SD}{PV_{bg}} x100\% \tag{4}$$

The PV_{abn}, PV_{bg} are the pixel values of the abnormalities and background, and σ_{bg} is the standard deviation of the background measured in a certain region of interest (ROI). The position of the ROIs is described in Section 3.2 and 3.3.

In order to evaluate the spatial resolution in each direction (x, y, and z), the metric *full width at half maximum* (FWHM) was used. The FWHM of the PV, SD, SDNR and C profiles were calculated. The FWHM were compared to the true geometry of the abnormalities. In calculating FWHM, Gaussian functions (5) were applied to interpolate the profile distribution. The FWHM was then determined by using equation (6).

$$f(x) = \frac{1}{\sigma\sqrt{2\pi}} e^{-\frac{(x-\mu)^2}{2\sigma^2}} \tag{5}$$

$$FWHM = 2.355\sigma \tag{6}$$

3. Results and discussion

3.1 Virtual breast phantom and its synthesized images

The voxel-based breast phantom adapted from breast CT data demonstrates realistic anatomical detail. In combination with the use of mathematical models, abnormality features can be further modified. The cross sections of the phantom viewed by the 3D viewer of ImageJ after fusion of abnormality and breast using the XRAYImagingSimulator software are shown in Figure 4. In this model, simulated abnormalities were added to an already compressed breast model. This approach was found appropriate, since a study by Zyganitidis et al. reported that the abnormalities maintain their shape and dimensions during compression, while the surrounding tissues (fat and gland) undergo considerable deformation and translation.[30]

With the 3D ImageJ viewer, it was possible to measure the dimensions of the abnormalities. They are listed in Table 3. Dimensions of microcalcifications after being voxelized have changed from their initial settings. This change was mainly due to the low resolution of the original breast images (0.27×0.27 mm^2) and thus the low resolution of the breast CT matrix which is a premise for digitization errors and rounding errors when transforming the ellipsoid to a voxel model. Data listed in the Table 3 were used as reference for the position and the size of ROIs for quantitative measurements. For comparing angular range and number of projections in DBT simulation, the image slice at Z = 0 is used for quantifying the irregular mass, while Z = -1mm and Z = 4 mm are used for quantifying *Calc1* and *Calc2* respectively.

The simulation of irradiation was also performed using the *XRAYImagingSimulator* software with addition of Poisson noise. The total dose applied for DBT was double to that used in 2D mammography. Simulated projection images with different noise level corresponding to different incident air kerma are shown in Figure 5(a-c). Specifically, Figure 5(a) corresponds to a 2D mammography image simulated for air kerma equal to 3.5 mGy, while Figure 5(b) and Figure 5(c) correspond to one projection image from the ±9° and ±25° DBT sets, respectively. In addition, Figure 5(d-h) and Figure 5(i-m) show reconstructed images for z = -1 mm (*Calc1*) and z = 4 mm (*Calc2*) for all DBT sets: ±9°, ±13°, ±15°, ±21° and ±25°.

3.2 The detectability of mass

A malignant lesion with irregular geometry was simulated. As mentioned above, the visibility of the mass is limited on 2D mammography due to the masking effect of dense background tissue. From verifying all our simulated images, the irregular mass can be recognized visually, and its margin can be determined by adjusting brightness and contrast level. Visualization of a mass in 2D mammography is easy for large and dense masses, when the breast is thin (not dense), and when optimal exposure parameters are chosen. It becomes gradually more difficult if all parameters are less optimal. In DBT image slices, the visualization of the irregular mass is better. These findings are confirmed by many studies which showed that a DBT system has superior performance in characterization and margin assessment of masses compared to digital mammography.[1,2,22-24] Variation of angular range and number of projection seems to weakly influence the visibility of the mass.

The ROIs for quantitative assessment are shown in Figure 6 and the calculated figures of merit at z = 0 (where the mass abnormality is centered) are listed in Table 4. The quantitative parameters between 2D mammography and DBT cannot be compared, since 2D mammography was evaluated in the projection image and DBT was evaluated using

reconstructed slices. All quantitative parameters show an increasing trend with increased angular range and number of projections in DBT simulation. Also the vertical direction was analyzed; the profiles of the mass in the 30 mm breast is shown in Figure 7. The FWHM values calculated from PV profiles were most deviating from the reference value (Table 3); they were in the range 302.8% to 525.7% respectively from the widest to smallest angular range. While from profiles of SD, SDNR and C, the deviations of FWHM values were respectively in the range 4.9% to 63.9%, 7.6% to 77.1%, and 5.6% to 63.2% respectively. The wider angular range and the use of figures of merit after background correction (SD, SDNR, and C) gave more accurate FWHM measurement. These values are summarized in Table 5.

Table 3. Position and dimensions of the abnormalities after insertion in a voxel-based breast phantom

Abnormality	*Center (mm)*			*Size (mm)*		
	Tube-travel	*Vertical*	*Front-back*	*Tube-travel*	*Vertical*	*Front-back*
Mass	4.9	0.3	-4.6	17.0	14.4	14.9
Calc1	5.4	-0.8	-4.9	0.8	0.3	0.8
Calc2	8.1	3.6	-4.9	0.8	0.5	0.8

Table 4. Mean pixel value, signal difference, SDNR and contrast of the irregular mass in the 2D mammography and DBT reconstructed slice at Z = 0.

System	*Mean pixel value*	*SD*	*SDNR*	*Contrast (%)*
2D Mammography	2.25	0.05	1.66	2.47
DBT ±9°, 10 proj	84.84	10.42	0.21	14.00
DBT ±13°, 14 proj	83.49	9.65	0.21	13.07
DBT ±15°, 16 proj	84.64	10.88	0.25	14.75
DBT ±21°, 22 proj	86.24	10.95	0.25	14.54
DBT ±25°, 26 proj	87.49	12.80	0.30	17.14

Table 5. Measurements of FWHM calculated using Gaussian interpolation of mean pixel value, signal difference, SDNR and contrast profiles of the irregular mass, together with their 95% confidence interval and coefficient of determination (R^2).

Projection angle	*Length (mm)*	*Mean Pixel Value*		*Signal difference*		*SDNR*		*% Contrast*	
		FWHM (mm)	R^2	*FWHM (mm)*	R^2	*FWHM (mm)*	R^2	*FWHM (mm)*	R^2
±9°	14.4	90.1[80.0-100.3]	0.80	23.6[21.1-26.2]	0.81	25.5[22.2-28.9]	0.74	23.5[21.0-26.1]	0.81
±13°	14.4	82.8[75.9-89.7]	0.88	21.9[19.7-24.0]	0.86	23.3[20.7-25.9]	0.82	21.9[19.7-24.1]	0.85
±15°	14.4	80.2[72.7-87.8]	0.85	19.7[17.7-21.7]	0.86	20.9[18.6-23.1]	0.84	19.8[17.8-21.8]	0.86
±21°	14.4	66.7[61.9-71.6]	0.90	16.9[15.3-18.5]	0.90	17.4[15.7-19.0]	0.90	17.0[15.4-18.7]	0.89
±25°	14.4	58.0[53.8-62.2]	0.90	15.1[13.3-16.9]	0.85	15.5[13.5-17.5]	0.83	15.2[13.4-17.0]	0.85

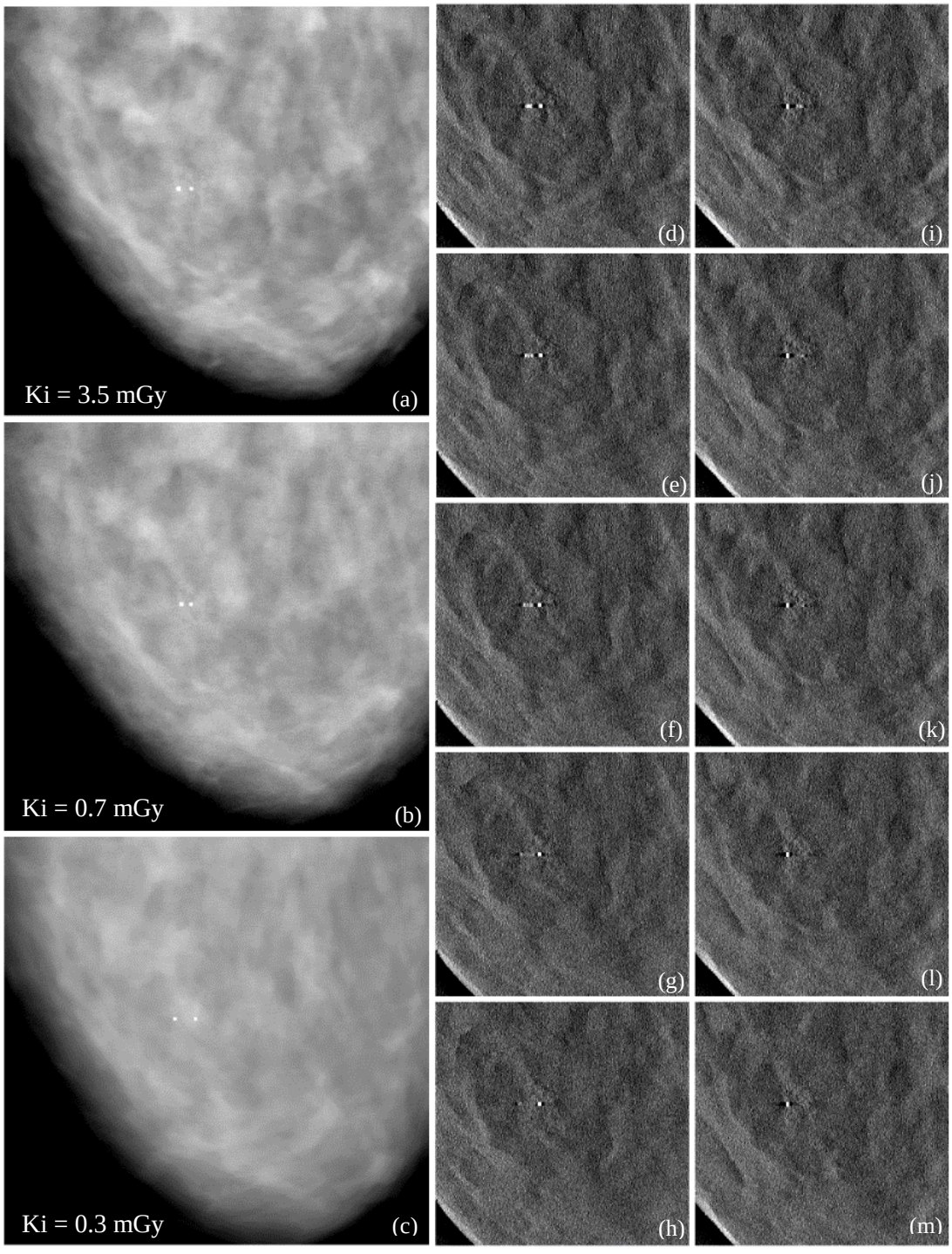

Figure 5. Some examples of projection images after the addition of noise for different projection angles of (a) 0°, (b) -9°, and (c) +25°; and reconstructed DBT slices based on acquisitions with angular range of ±9°, ±13°, ±15°, ±21°, and ±25° at z = -1 mm (d-h) and at z = 4 mm (i-m).

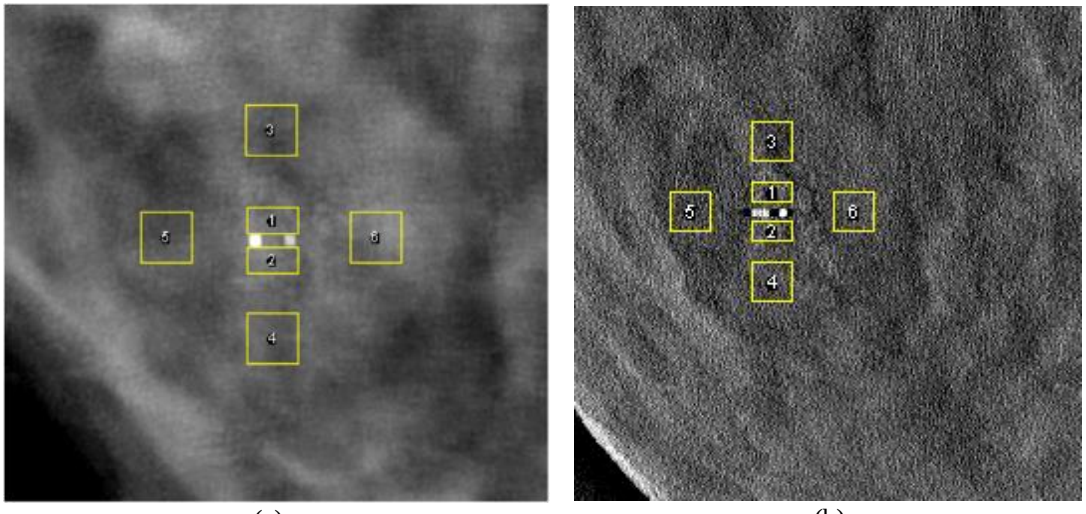

(a) (b)

Figure 6. ROIs settings for quantitative measurements of an irregular mass in (a) 2D Mammography and (b) a DBT reconstructed slice at Z = 0 from angular range of ±15° (16 projections). The ROI of the irregular mass was defined adjacent to and excluding the microcalcifications (region 1 and 2, with total dimension of 5.0 × 5.0 mm^2), while the breast tissue background was calculated from 4 squares surrounding the abnormality (region 3, 4, 5 and 6, with each dimension of 5.0 × 5.0 mm^2).

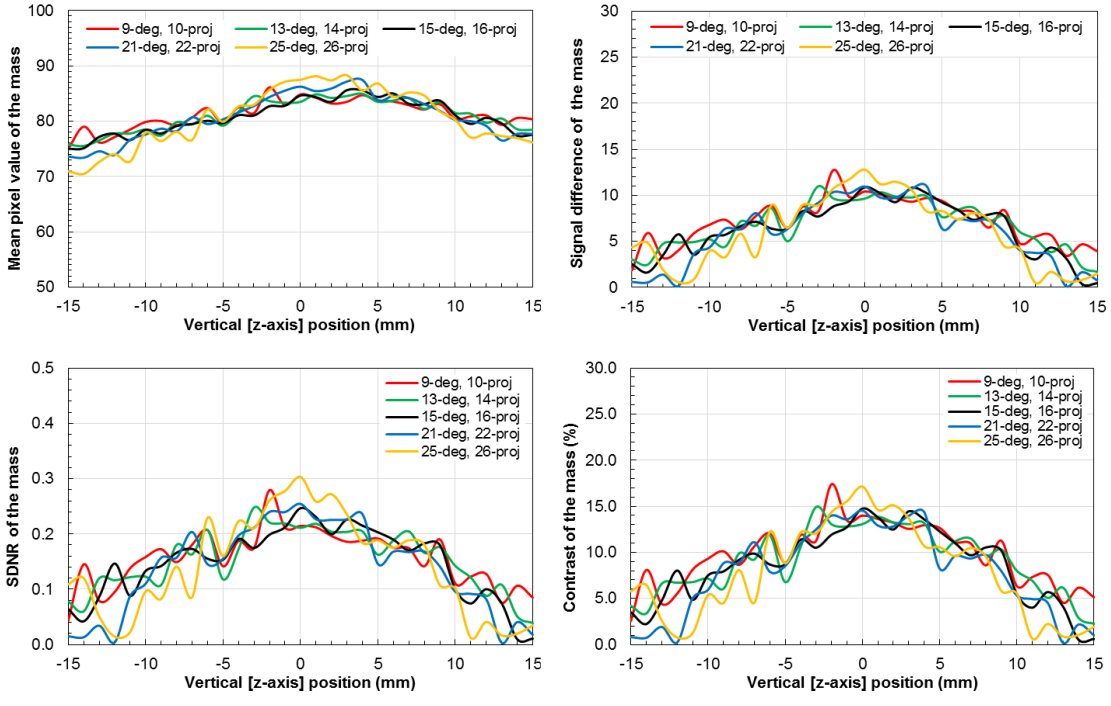

Figure 7. The profile of PV, SD, SDNR and C of irregular mass in vertical [z-axis] direction.

Table 6. Mean pixel value, signal difference, SDNR and contrast of microcalcification (*Calc1*) in 2D mammography system and DBT reconstructed slice at Z = -1 mm.

System	*Mean pixel value*	*SD*	*SDNR*	*Contrast (%)*
2D Mammography	2.5	0.2	9.1	10.1
DBT ±9°, 10 proj	254.7	179.4	4.0	238.3
DBT ±13°, 14 proj	251.9	174.3	4.2	224.7
DBT ±15°, 16 proj	251.7	172.9	4.1	219.6
DBT ±21°, 22 proj	251.4	169.8	4.7	208.3
DBT ±25°, 26 proj	253.4	169.2	5.9	201.0

3.3 The detectability of microcalcifications

A by qualitative analysis, microcalcifications can be seen clearly in both modalities, but there are artefacts visible in the DBT reconstructed images. Increasing the angular range and number of projections was found to reduce the artefacts.

Next to the four figures of merit, the FWHMs were also measured to evaluate the spatial geometry of the microcalcifications. Values of FWHM in coronal plane (in-plane) are obtained from a line profile, while the profile from certain regions are used for calculating the FWHM in z-axis. The pixel values used in the calculation were the mean value if the ROI is in fact a "region" and a single pixel value if the "line" was used. The choices made for the ROIs are shown in Figure 8.

The calculated figures of merit in coronal plane (in-plane direction for DBT system) for *Calc1* and *Calc2* are listed in Table 6 and Table 7, respectively. Similar with previous evaluations, the quantitative parameters of 2D mammography and DBT cannot be compared. The PV, SD and C of DBT images were not influenced by the variation of angular range and the number of projections, but the SDNR values show an increasing trend with increased angular range and number of projections.

In 2D mammography, the FWHM measurement from SD, SDNR and C gave similar results, since the same background ROIs were used. In each axis of the coronal plane, a FWHM of 0.9 mm was measured. That was 10% higher than the reference value. If applying PV for this measurement, the measured FWHM was 2.6 mm, or 182% higher than the reference value.

In evaluating in-plane spatial geometry of microcalcifications, the variation of angular range and number of projections had no impact on the FWHM measurement. For *Calc1*, PV line profile shows 0.8 mm and 1.0 mm at tube-travel and front-back direction respectively, while the three other figures of merit show 1.2 mm and 0.9 mm respectively. For *Calc2*, PV line profile shows 0.6 mm and 0.8 mm at tube-travel and front-back direction respectively, while the three others show 1.5 mm and 1.2 mm respectively. These results show that bias measurement by using PV is higher than SD, SDNR, and C where the true signals have been corrected by the background (Table 8 and Table 9).

In vertical direction of DBT images, the angular range and number of projections highly impact the spatial resolution. The profiles of PV, SD, SDNR, and C for *Calc1* in the range of 30 mm in Z-axis are shown in Figure 10.

3.4 Evaluation of the virtual tools

In Baneva *et al*, a study of breast structure was performed to validate the software framework. In the meantime, this framework has been expanded with more realistic noise sources to allow the study of the effect of dose. While a more detailed and stepwise validation should still be performed, the present study shows results in line with literature. Our results are encouraging with a view on future applications of the toolbox. Of course, it must always be taken in mind that the results arrive from a virtual world, and that practical applicability is limited by the models being implemented.

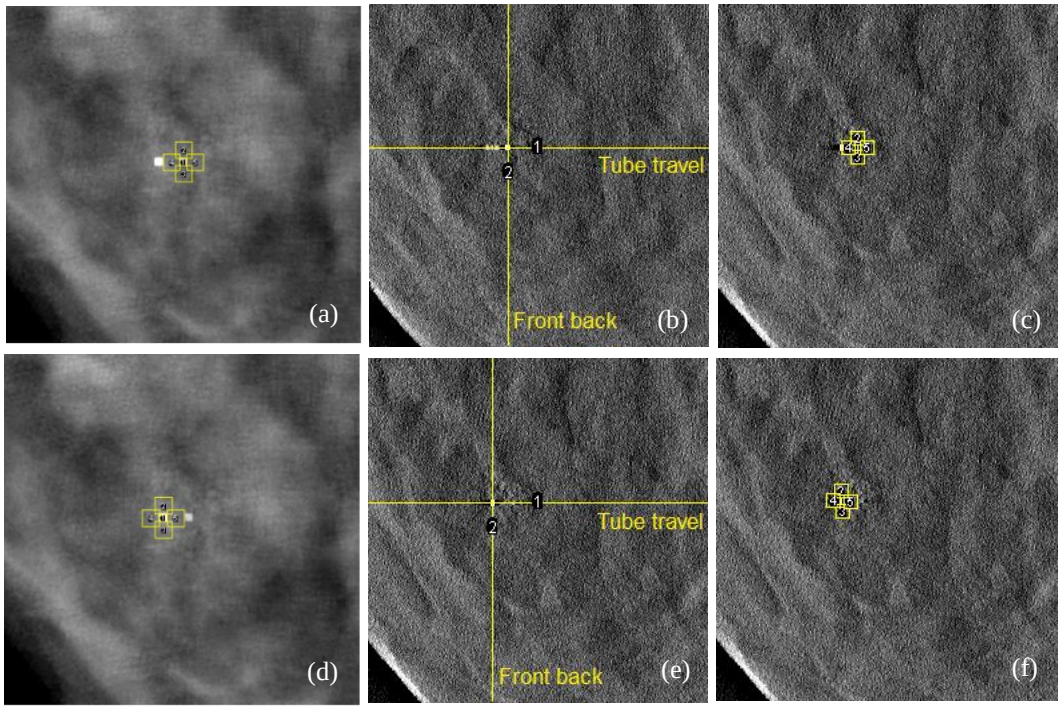

Figure 8. ROI settings for quantitative measurements of microcalcifications: *Calc1* is in the first row and *Calc2* is in the second one. The four figures of merits are measured within the region (a,d) for 2D Mammography and (c,f) for the DBT slices at Z = -1 mm for *Calc1* and Z = 4 mm for *Calc2*. The spatial geometry of the microcalcifications was measured in coronal plane along the line shown in (b,e), and in vertical direction for DBT images with ROIs setting as seen in (c,f): with dimension of 1.0 × 1.0 mm^2 for the target and four of squares (2.5 × 2.5 mm^2 each) for the background.

Table 7. Mean pixel value, signal difference, SDNR and contrast of microcalcification (*Calc2*) in 2D mammography system and DBT reconstructed slice at Z = 4 mm.

System	***Mean pixel value***	***SD***	***SDNR***	***Contrast (%)***
2D Mammography	2.9	0.6	13.5	27.1
DBT ±9°, 10 proj	255.0	177.1	3.8	227.1
DBT ±13°, 14 proj	253.2	178.4	4.2	238.6
DBT ±15°, 16 proj	255.0	183.2	4.6	255.2
DBT ±21°, 22 proj	254.5	179.9	4.7	241.1
DBT ±25°, 26 proj	249.9	175.0	4.7	233.8

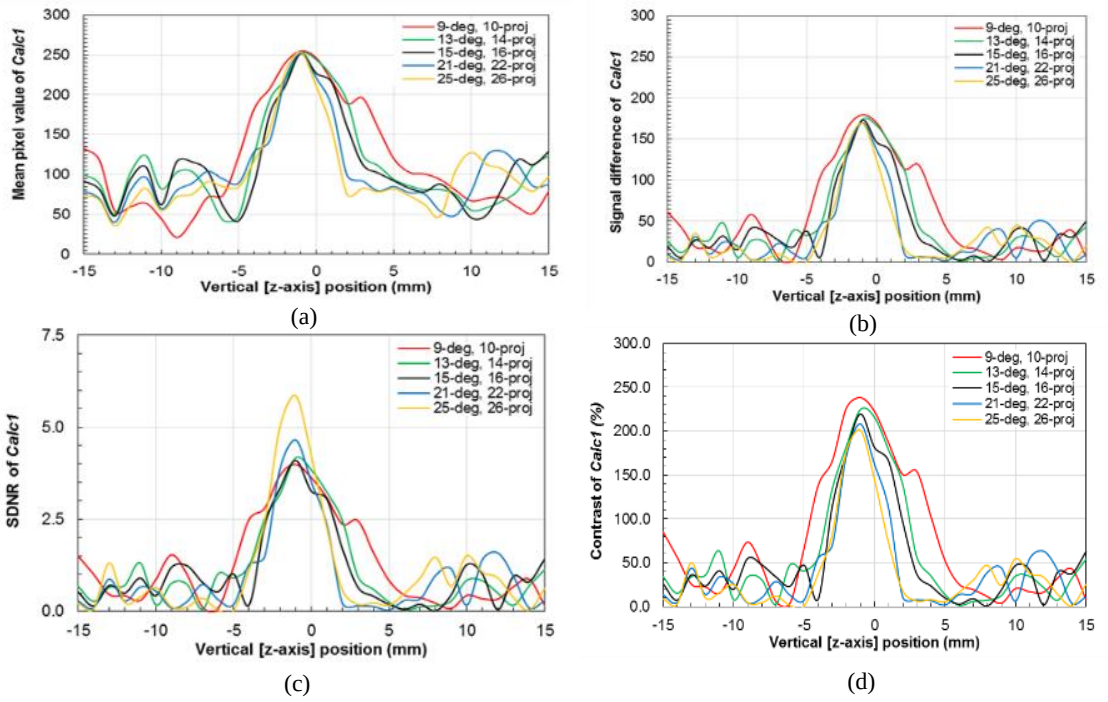

Figure 9. The profiles of PV, SD, SDNR, and C for *Calc1* in vertical [z-axis] direction.

Table 8. Measurement of FWHM calculated using Gaussian interpolation of mean pixel value, signal difference, SDNR and contrast profiles of *Calc1*, together with their 95% confidence interval and coefficient determination (R^2).

Projection angle	*Length (mm)*	*Mean Pixel Value*		*Signal difference*		*SDNR*		*% Contrast*	
		FWHM (mm)	R^2	*FWHM (mm)*	R^2	*FWHM (mm)*	R^2	*FWHM*	R^2
±9°	0.3	9.7 [8.2-11.1]	0.92	7.4 [6.0-8.8]	0.90	7.3 [5.9-8.6]	0.90	7.3 [5.9-8.6]	0.90
±13°	0.3	7.1 [6.3-7.9]	0.96	5.6 [5.0-6.3]	0.96	5.7 [4.9-6.4]	0.95	5.5 [4.9-6.2]	0.96
±15°	0.3	6.8 [5.8-7.7]	0.94	4.8 [3.9-5.7]	0.93	4.8 [3.9-5.8]	0.91	4.8 [3.9-5.6]	0.93
±21°	0.3	7.1 [5.7-8.5]	0.85	3.7 [3.2-4.3]	0.96	3.6 [3.0-4.2]	0.96	3.7 [3.1-4.2]	0.96
±25°	0.3	6.6 [5.2-7.9]	0.85	3.5 [3.3-3.7]	1.00	3.5 [3.3-3.7]	0.99	3.4 [3.2-3.6]	0.99

Table 9. Measurement of FWHM calculated using Gaussian interpolation of mean pixel value, signal difference, SDNR and contrast profiles of *Calc2*, together with their 95% confidence interval and coefficient determination (R^2).

Projection angle	*Length (mm)*	*Mean Pixel Value*		*Signal difference*		*SDNR*		*% Contrast*	
		FWHM (mm)	R^2	*FWHM (mm)*	R^2	*FWHM (mm)*	R^2	*FWHM*	R^2
±9°	0.5	15.9 [12.9-18.9]	0.84	11.9 [9.6-14.2]	0.85	11.3 [8.4-14.2]	0.76	10.6 [8.8-12.5]	0.87
±13°	0.5	10.0 [8.9-11.2]	0.95	7.4 [6.2-8.7]	0.91	7.1 [5.5-8.7]	0.85	7.1 [5.8-8.3]	0.91
±15°	0.5	8.9 [8.3-9.6]	0.98	6.4 [5.6-7.2]	0.96	6.1 [5.1-7.1]	0.93	6.0 [5.2-6.8]	0.96
±21°	0.5	8.3 [7.5-9.0]	0.96	5.4 [5.0-5.8]	0.99	5.1 [4.6-5.7]	0.98	5.2 [4.7-5.6]	0.98
±25°	0.5	7.4 [6.1-8.7]	0.89	4.2 [3.8-4.6]	0.98	4.0 [3.6-4.4]	0.98	4.0 [3.6-4.4]	0.98

4. Conclusion

Careful analysis of the simulated breast images showed that digital breast tomosynthesis has a greater potential for the detection of breast abnormalities than digital mammography. In our virtual study: varying the angular range of the DBT with similar incremental of the angular projection, it showed that the detectability of masses in coronal (in-plane) image was increased with increasing the angular range, while the detectability of microcalcifications was not influenced by the length of the acquisition arc. In vertical direction, the angular range and number of projections gave impact to all simulated abnormalities. These measurements show agreement with test results on real systems and underlines the value of simulation for better understanding and/or designing systems. This is especially encouraging if access to real data or real clinical studies is not possible or very expensive. In fact, a simulation framework made available to worldwide laboratories provides access to image data and optimization strategies.

Acknowledgements

This work is part of the homework for the Module MPE05 “Anthropomorphic phantoms” of the EUTEMPE-NET network 2017, supported by MaXIMA project: ‘Three dimensional breast cancer models for x-ray imaging research’. This project has received funding from the European Union’s Horizon 2020 research and innovation programme under grant agreement No 692097. We would also like to thank the Indonesia Endowment Fund for Education (LPDP) for the PhD grant of Kristina Tri Wigati.

References

[1] L. Cockmartin, N.W. Marshall, C. Van Ongeval, G. Aerts, D. Stalmans, F. Zanca, E. Shaheen, F. De Keyzer, D.R. Dance, K.C. Young, and H. Bosmans, "Comparison of digital breast tomosynthesis and 2D digital mammography using a hybrid performance test," Phys. Med. Biol. **60**, 3939–3958 (2015).

[2] E. Shaheen, C. Van Ongeval, F. De Keyzer, D.R. Dance, K.C. Young, and H. Bosmans, "The simulation of 3D mass models in 2D digital mammography and breast tomosynthesis," Med. Phys. **4**1(8), 081913 1–17 (2014).

[3] E. Shaheen, C. Van Ongeval, F. Zanca, L. Cockmartin, N. Marshall, J. Jacobs, K.C. Young, D.R. Dance, and H. Bosmans, "The simulation of 3D microcalcification cluster in 2D digital mammography and breast tomosynthesis," Med. Phys. **38**(12), 6659–6671 (2011).

[4] Y. Baneva, K. Bliznakova, L. Cockmartin, S. Marinov, I. Buliev, G. Mettivier, H. Bosmans, P. Russo, N. Marshall, and Z. Bliznakov, "Evaluation of a breast software model for 2D and 3D X-ray imaging studies of the breast," Phys. Med. (2017)

[5] X.G. Xu, "An exponential growth of computational phantom research in radiation protection, imaging, and radiotheraphy: a review of the fifty-year history," Phys. Med. Biol. **59**, R233–R302 (2014).

[6] L. Cockmartin, N.W. Marshall, G. Zhang, K. Lemmens, E. Shaheen, C. Van Ongeval, E. Fredenberg, D. R. Dance, E. Salvagnini, K. Michielsen, and H. Bosmans, "Design and application of a structured phantom for detection performance comparison between breast tomosynthesis and digital mammography," Phys. Med. Biol. **62**, 758–780 (2017).

[7] A. Taibi, S. Fabbri, P. Baldelli, C. di Maggio, G. Gennaro, M. Marziani, A. Tuffanelli, and M. Gambaccini, "Dual-energy imaging in full-field digital mammography: a phantom study," Phys. Med. Biol. **48**, 1945–1956 (2003).

[8] L.C. Ikejimba, S. J. Glick, K.R. Choudhury, E. Samei, and J.Y. Lo, "Assessing task performance in FFDM, DBT, and synthetic mammography using uniform and anthropomorphic physical phantoms," Med. Phys. **43**(10), 5593–5602 (2016).

[9] L. Cockmartin, H. Bosmans, and N.W. Marshall, "Comparative power law analysis of structured breast phantom and patient images in digital mammography and breast tomosynthesis," Med. Phys. **40**(8), 081920 1–17 (2013).

[10] H. Zaidi and B.M.W. Tsui, "Review of computational anthropomorphic anatomical and physiological models," Proceedings of the IEEE **97**(12), 1938–1953 (2009).

[11] D.D. Pokrajac, A.D.A. Maidment, and P.R. Bakic, "Optimized generation of high resolution breast anthropomorphic software phantoms," Med. Phys. **39**(4), 2290–2302 (2012).

[12] N. Kiarashi, A.C. Nolte, G.M. Sturgeon, W.P. Segars, S.V. Ghate, L.W. Nolte, and E. Samei, "Development of realistic physical breast phantoms matched to virtual breast phantoms based on human subject data," Med. Phys. **42**(7), 4116–4126 (2015).

[13] A.K. Carton, P. Bakic, C. Ullberg, H. Derand, and A.D.A. Maidment, "Development of a physical 3D anthropomorphic breast4

[14] C.M. Li, W.P. Segars, G.D. Tourassi, J.M. Boone, and J.T. Dobbins III, "Methodology for generating a 3D computerized breast phantom from empirical data," Med. Phys. **36**(7), 3122–3131 (2009).

[15] K. Bliznakova, Z. Bliznakov, V. Bravou, Z. Kolitsi, and N. Pallikarakis, "A three-dimensional breast software phantom for mammography simulation," Phys. Med. Biol. **48**, 3699–3719 (2003).

[16] K. Bliznakova, S. Kazakli, and N. Pallikarakis, "An optimised 3D breast phantom for X-ray breast imaging techniques," IFMBE Proceedings **22**, 2455–2458 (2008).

[17] K. Bliznakova, S. Suryanarayanan, A. Karellas, and N. Pallikarakis, "Evaluation of an improved algorithm for producing realistic 3D breast software phantoms: application for mammography," Med. Phys. **37**(11), 5604–5617 (2010).

[18] P.R. Bakic, M. Albert, D. Brzakovic, and A.D.A. Maidment, "Mammogram synthesis using a 3D simulation. I. Breast tissue model and image acquisition simulation," Med. Phys. **29**(9), 2131–2139 (2002).

[19] P.R. Bakic, M. Albert, D. Brzakovic, and A.D.A. Maidment, "Mammogram synthesis using a 3D simulation. II. Evaluation of synthetic mammogram texture," Med. Phys. **29**(9), 2140–2151 (2002).

[20] P.R. Bakic, M. Albert, D. Brzakovic, and A.D.A. Maidment, "Mammogram synthesis using a 3D simulation. III. Modelling and evaluation of the breast ductal network," Med. Phys. **30**(7), 1914–1925 (2003).

[21] B. Chen, J. Shorey, R.S. Saunders, S. Richard, J. Thompson, L.W. Nolte, and E. Samei, "An anthropomorphic breast model for breast imaging simulation and optimization," Acad. Radiol. **18**, 536–546 (2011).

[22] I. Sechopoulos, "A review of breast tomosynthesis. Part I. The image acquisition process," Med. Phys. **40**(1), 014301 1–12 (2013).

[23] I. Sechopoulos, "A review of breast tomosynthesis. Part II. Image reconstruction, processing and analysis, and advanced applications," Med. Phys. **40**(1), 014302 1–17 (2013).

[24] D. R. Dance, S. Christofides, A. D. A. Maidment, I. D. McLean, and K. H. Ng, "Diagnostic Radiology Physics: A handbook for teachers and students," IAEA (2014).

[25] K. Bliznakova, R. Speller, J. Horrocks, P. Liaparinos, Z. Kolitsi, N. Pallikarakis, "Experimental validation of a radiographic simulation code using breast phantom for x-ray imaging," Comput. Biol. Med. **40**, 208–214 (2014).

[26] X. Yang, I. Sechopoulos, and B. Fei, "Automatic tissue classification breast CT images based on bilateral filtering," Proc. SPIE 7962: 79623H (2011).

[27] H. Hintsala, K. Bliznakova, N. Pallikarakis, and T. Jämsä, "Modelling of Irregular Breast Lesions," IFMBE Proc. **25**(IV), 2024–2027 (2009).

[28] D. Lazos, Z. Kolitsi, and N. Pallikarakis, "A software data generator for radiographic imaging investigations," IEEE Trans. Inf. Technol. Biomed. **4**(1), 76–79 (2000).

[29] L.A. Feldkamp, L.C. Davis, and J.W. Kress, "Parctical cone-beam algorithm," J. Opt. Soc. Am. **1**(6), 612–619 (1984).

[30] C. Zyganitidis, K. Bliznakova, and N. Pallikarakis, "A novel simulation algorithm for soft tissue compression," Med. Bio. Eng. Comput. **45**: 661–669 (2007).